

Article

Nanocomposite Electrode of Titanium Dioxide Nanoribbons and Multiwalled Carbon Nanotubes for Energy Storage

Mohammad BinSabt¹, Mohamed Shaban^{2,3,*}  and Ahmed Gamal³¹ Chemistry Department, Faculty of Science, Kuwait University, P.O. Box 5969, Safat 13060, Kuwait² Department of Physics, Faculty of Science, Islamic University of Madinah, P.O. Box 170, Madinah 42351, Saudi Arabia³ Nanophotonics and Applications Laboratory, Physics Department, Faculty of Science, Beni-Suef University, Beni-Suef 62514, Egypt

* Correspondence: mssfadel@aucegypt.edu

Abstract: TiO₂ is one of the most investigated materials due to its abundance, lack of toxicity, high faradaic capacitance, and high chemical and physical stability; however, its potential use in energy storage devices is constrained by its high internal resistance and weak van der Waals interaction between the particles. Carbon nanotubes are especially well suited for solving these issues due to their strong mechanical strength, superior electrical conductivity, high electron mobilities, excellent chemical and thermal stability, and enormous specific nanoporous surface. The hydrothermal approach was followed by chemical vapor deposition to produce a network composite of titanium dioxide nanoribbons (TNRs) and multi-walled carbon nanotubes (MWCNTs). The nanocomposite was characterized using a variety of methods. One phase of TiO₂-B nanoribbons has porous pits on its surface, and MWCNTs are grown in these pits to produce a network-like structure in the nanocomposite. With a two-electrode supercapacitor configuration, the TNR/CNT gave a gravimetric capacitance of 33.33 F g⁻¹, which was enhanced to 68.18 F g⁻¹ in a redox-active electrolyte containing hydroquinone (HQ). Additionally, the areal capacitance per footprint was increased from 80 mF cm⁻² in H₂SO₄ to 163.63 mF cm⁻² in H₂SO₄/HQ. The TNR/CNT supercapacitor has superior cyclic stability than the previously reported TiO₂-based electrodes, with 97.5% capacitance retention after 5000 cycles. Based on these results, it looks like the TNR/CNT supercapacitor could provide portable electronic power supplies with new ways to work in the future.

Keywords: nanocomposite; supercapacitor; TiO₂; CNTs; energy storage

Citation: BinSabt, M.; Shaban, M.; Gamal, A. Nanocomposite Electrode of Titanium Dioxide Nanoribbons and Multiwalled Carbon Nanotubes for Energy Storage. *Materials* **2023**, *16*, 595. <https://doi.org/10.3390/ma16020595>

Academic Editors: Junwei Wu and Yanan Chen

Received: 19 October 2022

Revised: 31 October 2022

Accepted: 7 November 2022

Published: 7 January 2023



Copyright: © 2023 by the authors. Licensee MDPI, Basel, Switzerland. This article is an open access article distributed under the terms and conditions of the Creative Commons Attribution (CC BY) license (<https://creativecommons.org/licenses/by/4.0/>).

1. Introduction

Portable smart devices could benefit from supercapacitors because of their fast discharge speed, long cycle life, and high-power density, among other advantages. In terms of energy storage, supercapacitors are divided into electrochemical double-layer capacitors with higher power density linked to the electrode surface area and pseudocapacitors with higher energy density linked to faradaic redox [1]. High-performance electrode materials for supercapacitors have mostly been developed by modifying and blending pseudocapacitive materials such as transition metal oxides and conductive polymers with carbonaceous materials from double-layer capacitors [2,3]. As electrodes for supercapacitors, carbon nanotube electrodes have proven to retain the remarkable qualities of individual carbon nanotubes while also exhibiting good mechanical properties and structural stability [4,5]. This study also examined the properties of titanium dioxide (TiO₂), which has a high faradaic capacitance and is chemically and physically stable [6]. Despite this, TiO₂'s high internal resistance prevents it from being used in an energy storage device. Due to the weak van der Waals interaction between the particles, TiO₂ has not yet been successfully used as an electrode in a supercapacitor, but it can be combined with other materials, particularly carbon-based materials. As shown in Table 1, previous studies on TiO₂/activated carbon,

TiO₂/carbon nanotubes, and reduced graphene oxide/TiO₂ nanobelt composites revealed that the combination of conductive nanocarbon and TiO₂ was an efficient solution [7–15]. Selvakumar and Bhat developed TiO₂/activated carbon nanocomposite electrodes, which have a specific capacitance of 122 F/g at current densities of 2, 4, 6, and 7 mA/cm² [7]. A PANI/TiO₂/GO composite with high specific capacitance—1020 F/g at 2 mV/s and 430 F/g at 1 A/g—was made by Su et al. [8]. The rGO-TiO₂ nanobelts and nanoparticles made by Xiang et al. had specific capacitances of 225 and 62.8 F/g, respectively. Ramadoss et al. produced an rGO/TiO₂ NR/rGO electrode with 114.5 F/g at a scan rate of 5 mV/s that maintained more than 85% of its initial capacitance after 4000 cycles [10]. Ramadoss and Kim used a microwave-assisted technique to produce a graphene–TiO₂ hybrid nanostructure with a specific capacitance of 165 F/g at a scan rate of 5 mV/s in a 1 M Na₂SO₄ solution and retention of 90% specific capacitance after 5000 cycles [11]. High specific and interfacial capacitances, of 329 F/g and 52 mF/cm² at a scan rate of 5 mV/s were achieved by coating TiO₂ nanodots on MWCNTs using a binder-free method developed by Sankapal et al. [12]. Using a sacrificial template technique, Ke et al. produced a 3D carbon/TiO₂/rGO composite with a specific capacitance of 23.6 mF/cm² [13]. In a 0.5 M H₂SO₄ electrolyte, the TiO₂/CNT hybrid produced by Yan et al. using the sol–gel technique exhibits a specific supercapacitance of 145 F/g [14]. By co-electrochemically reducing functionalized MWCNTs and GO onto TiO₂NTs/Ti, Faraji created a 3D R(fMWCNT-GO)/TiO₂NTs/Ti electrode with a specific capacitance of 600 F/g at 12 A/g in 1 M H₂SO₄ and a long cycle life of 90% capacitance retention over 500 cycles [15]. Despite previous research, it is urgent to create TiO₂/carbon-based nanocomposite electrodes for supercapacitors that are less expensive, have a high yield and surface area, and are more stable.

Table 1. The CNTs and nanocomposite’s crystallite sizes (CS), d-spacing, dislocation densities, texture coefficients, and strain.

Peaks	2θ (Deg)	CNTs				TNRs/CNTs					
						CNTs			TiO ₂ —B		
	Planes	26.32	42.91	44.94	65.74	26.35	44.05	53.48	33.0020	47.7603	67.0194
		(002)	(100)	(101)	(004)	(002)	(101)	(004)	(310)	(−512)	(711)
	CS (Å)	146.78	153.56	177.04	106.52	168.03	154.18	63.74	99.09	156.31	113.98
	d-spacing (Å)	3.386	2.108	2.017	1.705	3.383	2.056	1.713	2.714	1.904	1.396
	Dislocation density (δ) × 10 ^{−5} (Å ^{−2})	4.64	4.24	3.19	8.81	3.54	4.21	24.61	10.18	4.09	7.70
	Texture Coefficient (TC)	2.538	0.442	0.895	0.125	2.275	0.562	0.163	0.875	1.579	0.546
	Microstrain only (%)	1.154	0.686	0.570	0.800	1.006	0.667	1.344	1.370	0.609	0.6126

The hydrothermal approach was used in this study to achieve the controllability of TiO₂ structures in a simple, low-cost method while also significantly increasing the energy storage capacity of the electrode materials. Metal carbides will be used more in energy storage devices as a result of this. The TiO₂ nanoribbon acts as a substrate for the chemical vapor deposition (CVD) of carbon nanotubes on its surface. In various solutions, electrochemical impedance spectroscopy (EIS), cyclic voltammetry (CV), and galvanostatic charge/discharge (GCD) were used to measure the nanocomposite performance. Their capacity, specific power, and specific energy were also investigated to evaluate how well they will operate over 5000 cycles of reusability.

2. Experimental Section

2.1. Materials

Loba Chemie (Mumbai, India) provided the TiO₂ powder (Loba Chemie, India, CAS No. 13463-67-7), Fe (NO₃)₃·9H₂O (Loba Chemie, India, CAS No. 7782-61-8), Co(NO₃)₂·H₂O (Loba Chemie, India, CAS No. 10026-22-9), and Al(NO₃)₃·9H₂O (Loba Chemie, India, CAS No. 7784-27-2). Scharlab (Barcelona, Spain) supplied HCl (36.6%). SDFCL (Mumbai, India)

supplied H_2SO_4 (98%) and HNO_3 (69%). Deliveries from ADWIC (Cairo, Egypt) included commercial C_2H_4 gas, NH_4OH (32%) and NaOH .

2.2. TNRs/CNTs Nanocomposite Fabrication

TNRs were made using an alkaline hydrothermal process. In 400 mL of 10 M NaOH , 4 gm of TiO_2 powder was added and stirred for 30 min. In a 1 L autoclave, the resulting solution was poured. The autoclave was then placed in a 170 °C oven for 24 h. The result was then filtered before being washed with 0.1 M HCl and distilled water. Finally, the white powder was dried for 4 h at 80 °C and calcined for 2 h at 450 °C [16].

The TiO_2 nanoribbons were mixed with $\text{Fe}(\text{NO}_3)_3 \cdot 9\text{H}_2\text{O}$, $\text{Co}(\text{NO}_3)_2 \cdot 6\text{H}_2\text{O}$, and $\text{Al}(\text{NO}_3)_3 \cdot 9\text{H}_2\text{O}$ in 100 mL of distilled water under stirring, with mass ratios of 10 TiO_2 :20 Fe:20 Co:50 Al_2O_3 . By slowly drizzling in drops of ammonia solution, the pH level rose to 8 and the precipitation occurred. The solution was filtered and rinsed with distilled water. The solution was aged for 2 h at room temperature. To eliminate excess nitrate, the product was first dried for 4 h at 80 °C and then calcined for 4 h at 450 °C [17].

The functionalized titanium nanoribbons were used as a catalyst for the formation of CNTs using tubular chemical vapor deposition (CVD). The carbon source was C_2H_4 , and the carrier gas was N_2 . $\text{C}_2\text{H}_4:\text{N}_2$ was a 1:10 *v/v* ratio. The CNTs were grown for 50 min at 700 °C [18]. For 6 h at 120 °C, we heated the CVD-prepared product in a round bottom flask to dilute it with $\text{H}_2\text{SO}_4:\text{HNO}_3$ (1:3). Next, the powder was cleaned and dried at 80 °C for 4 h using distilled water [19,20]. A total of 1 g of the composite is expected to cost between \$5 and \$6.

2.3. Characterization of the Produced Nanomaterials

X-ray diffraction (XRD; PANalytical, Warsaw, Poland) using $\text{Cu K}\alpha$ radiation ($\lambda = 1.5406 \text{ \AA}$) at 45 kV and 40 mA validated the crystal structure of the CNTs and TNRs/CNTs. A transmission electron microscope (TEM) was used to examine the morphologies of the produced nanocomposites (JEOL JEM-2100 TEM, Tokyo, Japan).

2.4. Supercapacitor Manufacturing Processes

A total of 20 mg of active material powder and 50 μL of Nafion were dispersed in 300 μL of ethanol and then blended into a slurry in a smaller agate mortar. To make a homogenous catalyst ink, the mixture was agitated for 12 h. On the Au electrode, two identical slurries of about 50 μL (3 mg) were placed (1 cm^2). Two sheets of filter paper, on the other hand, were dipped in electrolytes, which may be either 1 M H_2SO_4 or a mixture of 1 M H_2SO_4 and 0.4 M hydroquinone (HQ) ($\text{H}_2\text{SO}_4/\text{HQ}$). After that, a sheet of filter paper was placed between the two electrodes as a separator.

2.5. Electrochemical Analysis

All electrochemical measurements in the two-electrode systems were performed using an electrochemical workstation (CHI 660E; CH Instruments, Austin, TX, USA). Cyclic voltammetry (CV), galvanostatic charge/discharge (GCD), and electrochemical impedance spectroscopy (EIS) were used to make the measurements. The CV experiments were carried out at various scan rates between 0 and 1 V, ranging from 5 to 100 mV s^{-1} . The GCD measurements were carried out in a voltage window of 0 to 1 V at 0.2–1 A g^{-1} . The EIS spectra were recorded at an open circuit potential of 5 mV AC voltage amplitude and frequencies ranging from 10 mHz to 100 kHz. The tests were all conducted at room temperature.

3. Results and Discussions

3.1. Characterization of the Produced Nanomaterials

3.1.1. Structural Properties

XRD spectroscopy was used to analyze the TNR/CNT nanocomposite and identify its crystal structure. The XRD charts for the nanocomposite CNTs and TNRs/CNTs are displayed in Figure 1. A strong peak associated with XRD diffraction from the (002) plane

can be seen on the CNTs chart at 26.32° . In addition, the peaks at 42.91° and 44.94° are connected to the carbon's in-plane (100) and (101) reflections, respectively, while the peak at 65.74° is connected to the XRD from (004) [21].

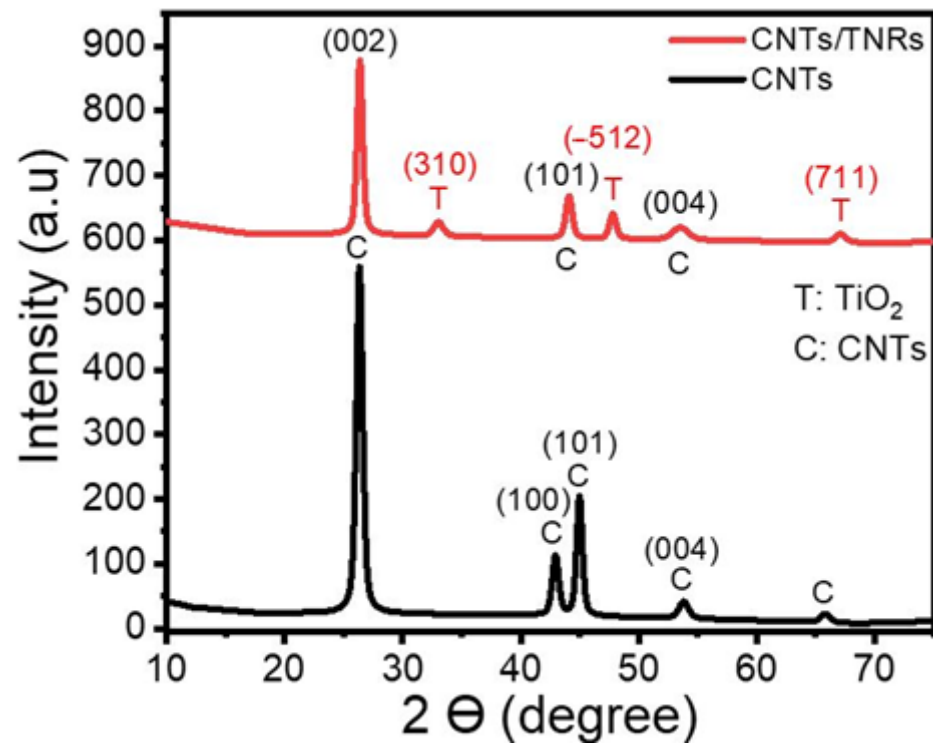


Figure 1. The XRD pattern of a TNR/CNT nanocomposite.

The XRD pattern of TNRs/CNTs exhibited three unique CNT peaks at $2\theta = 26.34^\circ$, 44.05° , and 53.48° , in the (002), (101), and (004) planes, respectively [17]. Additionally, $\text{TiO}_2\text{-B}$ is associated with the peaks in the Figure 1 planes (310), (−512), and (711) at 33.0° , 47.76° , and 67.02° [22–24].

The average crystallite size, CS, was determined using the Scherrer equation $CS = \frac{0.9\lambda}{\beta \cos\theta}$ where β is the full width at half maximum (FWHM); θ is the Bragg's angle in radians; and λ is the X-ray wavelength ($\text{CuK}\alpha = 0.15405 \text{ nm}$) [25,26]. Additionally, the dislocation density (δ) was determined by applying Williamson and Smallman's relation, where $N = 1$ represents the minimum dislocation density and $\delta = \frac{N}{CS^2}$. Using Equation (1), the texture coefficient (TC) was also calculated from the data [25,26].

$$TC(hkl) = \frac{I_r(hkl)}{\frac{1}{N} \sum I_r(hkl)} \quad (1)$$

where N is the number of reflections and $I_r = \frac{I(hkl)}{I_0(hkl)}$ is the difference between the measured intensity $I(hkl)$ and the standard intensity $I_0(hkl)$ for the plane hkl .

Table 1 contains the computed and actual values for the CNTs and the nanocomposite's crystallite sizes (CS), d-spacing, dislocation densities, texture coefficients, and microstrain. Growing CNTs on the surface of TNRs resulted in an increase in the crystallite size of CNTs along (002) from 14.7 nm to 16.8 nm. TNRs typically have crystallite sizes between (−512) and (310) of 15.6 and 9.9 nm, respectively. Based on the values of the texture coefficient in Table 1, the preferred orientations for $\text{TiO}_2\text{-B}$ (TNRs) and CNTs were (−512) and (002), respectively. Additionally, the (−512) and (002) planes had lower TNR and CNT dislocation densities than the other planes. This is brought on by the grains along these planes having a higher crystallinity [27]. Table 1 reports the positive microstrain values, which indicate a

lattice expansion and relaxation [28]. The CNTs in the pure sample and the composite are reported to have the highest values of microstrain along the (002).

3.1.2. Morphological Analysis

TEM was used to analyze the nanocomposite's morphology. As illustrated in Figure 2a, the CVD-grown CNTs formed multi-walled carbon nanotubes (MWCNTs), with the inner and outer tubes having widths of 5 to 7 nm and 15 to 17 nm, respectively. TiO₂ nanoribbons have a structure that is wider, longer, and straighter. The nanoribbons' typical width ranged from 20 to 200 nm. As illustrated in Figure 2b, these nanoribbons have a dense distribution of nano pits on their surfaces. The nano pits have a diameter ranging from 4 to 8 nm [29]. As seen in the inset figure, the nanoribbon works as a substrate for the growth of carbon nanotubes on its surface.

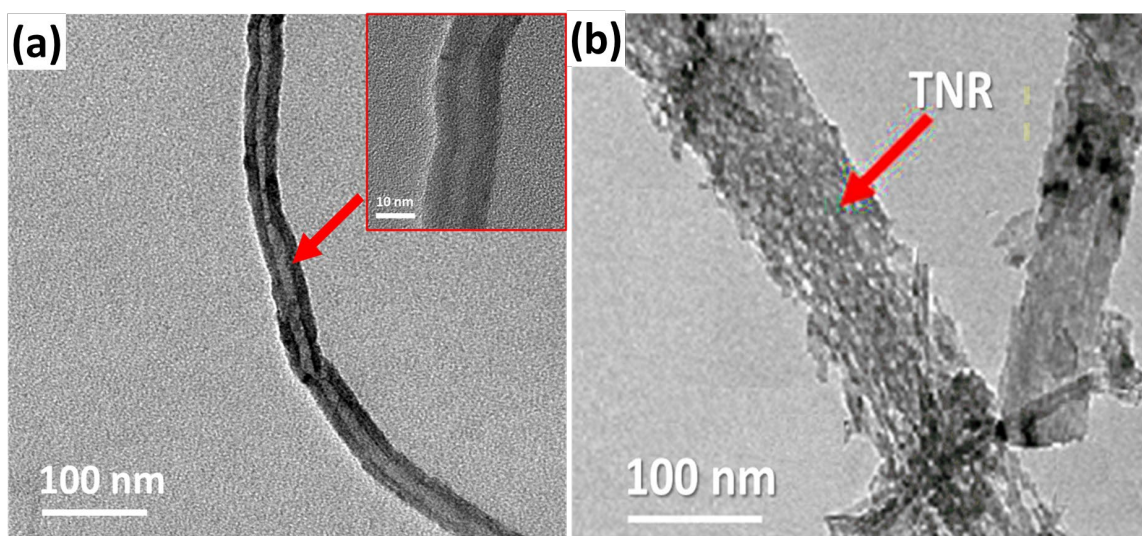


Figure 2. TEM pictures of (a) the CNTs and the (b) TNR/CNT nanocomposite.

3.2. TNR/CNT Nanocomposite Electrochemical Performance in 1 M H₂SO₄

Any material's capacitive behavior can be measured using cyclic voltammetry. CV was performed on a symmetric supercapacitor cell made in a sandwich-type geometry utilizing TNR/CNT electrodes, paper as a separator, and 1 M H₂SO₄ as an electrolyte to study the capacitive properties of TNR/CNTs, and the results were compared to those of CNTs. Figure 3a shows the cyclic voltammograms produced for TNRs/CNTs and CNTs at 10 mV s⁻¹. Figure 3a shows the electrodes' outstanding stability over the applied voltage range of 0 to 1 V. Using the formula [30], the specific capacitance was determined from the voltammograms.

$$C_s = \frac{2 \times i}{m \times v} \quad (2)$$

where C_s is the specific capacitance found from the CV; ' i ' is the average current found from the anodic and cathodic curves; v gives the scan rate; and m is the weight of the active material in one electrode. The CNTs' cyclic voltammograms are quasi-rectangular along the x-axis, with a small redox peak, in the beginning, showing that they have both double-layer and pseudocapacitance behavior. Because of the widespread oxidation of CNTs, oxidizable groups such as hydroxyl, carbonyl, and carboxyl are formed at defects in the nanotube carbon lattice, resulting in pseudocapacitance [30]. However, when TiO₂ and the CNTs worked together, the TNR/CNTs showed an improved rectangular background and oxide peak.

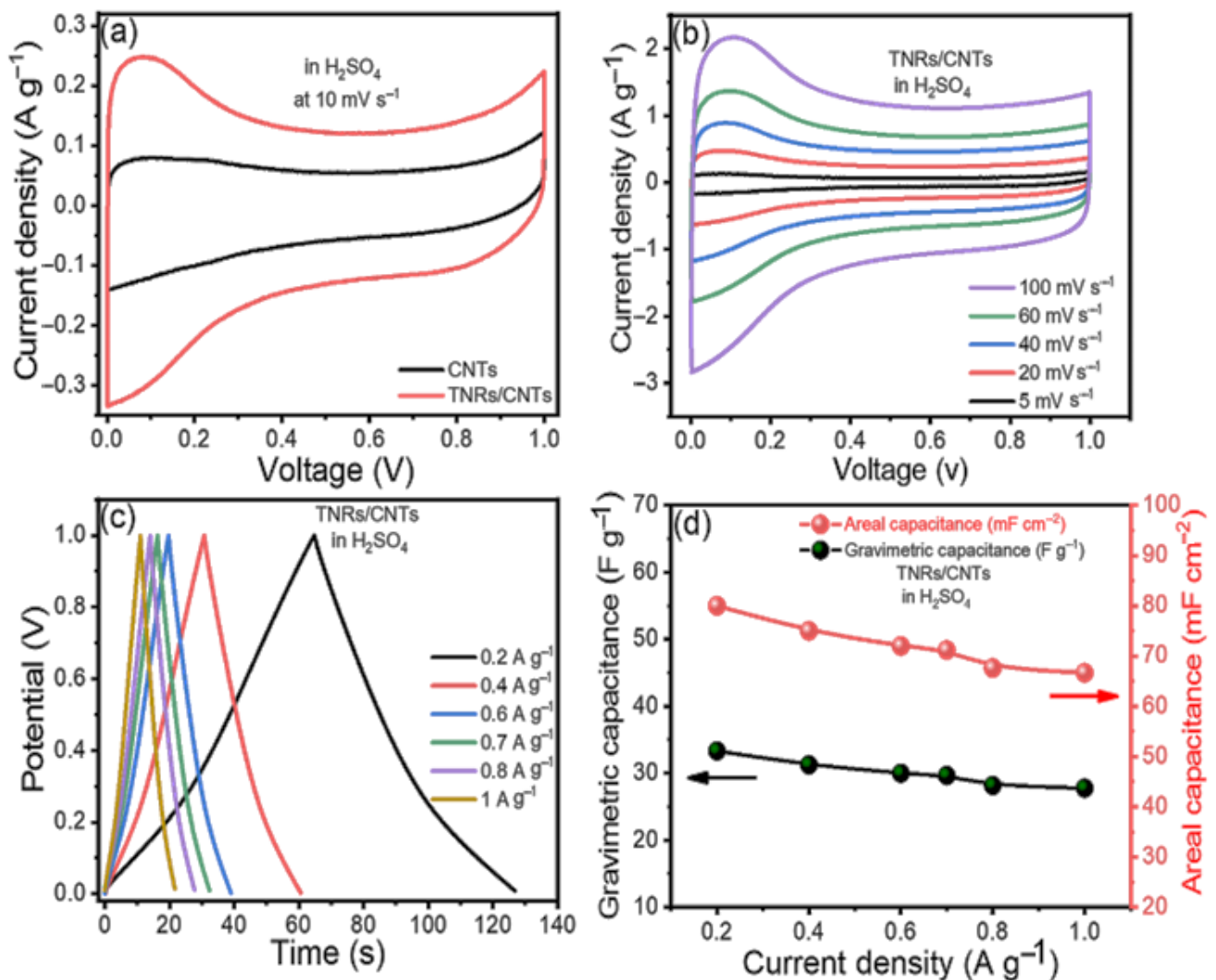


Figure 3. The electrochemical performance of the TNR/CNT electrodes in the H_2SO_4 (a) cyclic voltammograms (CVs) of the CNTs and TNR/CNTs at a scan rate of 10 mV s^{-1} , (b) CVs at different scan rates, (c) charge/discharge curves (CDs) at different current densities, and (d) computed gravimetric and areal capacitances at different current densities.

The TNR/CNTs performance was also assessed at various scan rates; Figure 3b shows the fluctuation of C_s with the scan rate. Because the redox reactions in TNR are dependent on the insertion–deinsertion of dopant ions from the electrolyte, the C_s values fall as the scan rate increases [31,32]. At low scan rates, ions from the electrolyte can move into almost all of the material’s pores. This causes a complete insertion reaction and the most capacitive behavior possible.

The CD curves of the TNR/CNT electrodes at different scan rates are shown in Figure 3c; the divergence from linearity is due to the pseudocapacitance from TNR. The longer charge and discharge times are due to the use of EDLC and faradic capacitance from TNRs and CNTs, respectively.

Figure 3d illustrates the supercapacitor’s gravimetric (C_{wt}) and areal (C_A) capacitances at various current densities, as derived from the charge/discharge curves using the following equations [33,34].

$$C_{wt} = \frac{4I}{m \left(\frac{\Delta E}{\Delta t} \right)} \quad (3)$$

$$C_A = \frac{4I}{A \left(\frac{\Delta E}{\Delta t} \right)} \quad (4)$$

where “ I ” represents the applied constant current (A); $\left(\frac{\Delta E}{\Delta t} \right)$ is the slope of the discharge curve; the two electrodes’ footprint area (cm^2) is marked by A ; and the total mass of the two electrodes is given by m (g).

At a current density of 0.2 A g^{-1} , the gravimetric capacitance in H_2SO_4 reached its maximum value of 33.33 F g^{-1} . As the current density decreased, the device’s area capacitance increased from 66.66 mF cm^{-2} to 80 mF cm^{-2} . Choosing an electrolyte mixture improved the performance of our electrodes.

3.3. The TNR/CNTs Electrode’s Superior Performance

Hydroquinone (HQ) was added to $1 \text{ M H}_2\text{SO}_4$ to make a mixed electrolyte since it was believed to be an effective redox-active electrolyte that provided additional redox reactions [35]. Using a mixed electrolyte significantly enhanced the cyclic voltammetry integrated area (Figure 4a). In Figure 4b, the electrolyte had the longest CD duration, and the fact that it did not look like a triangle suggests that HQ is involved.

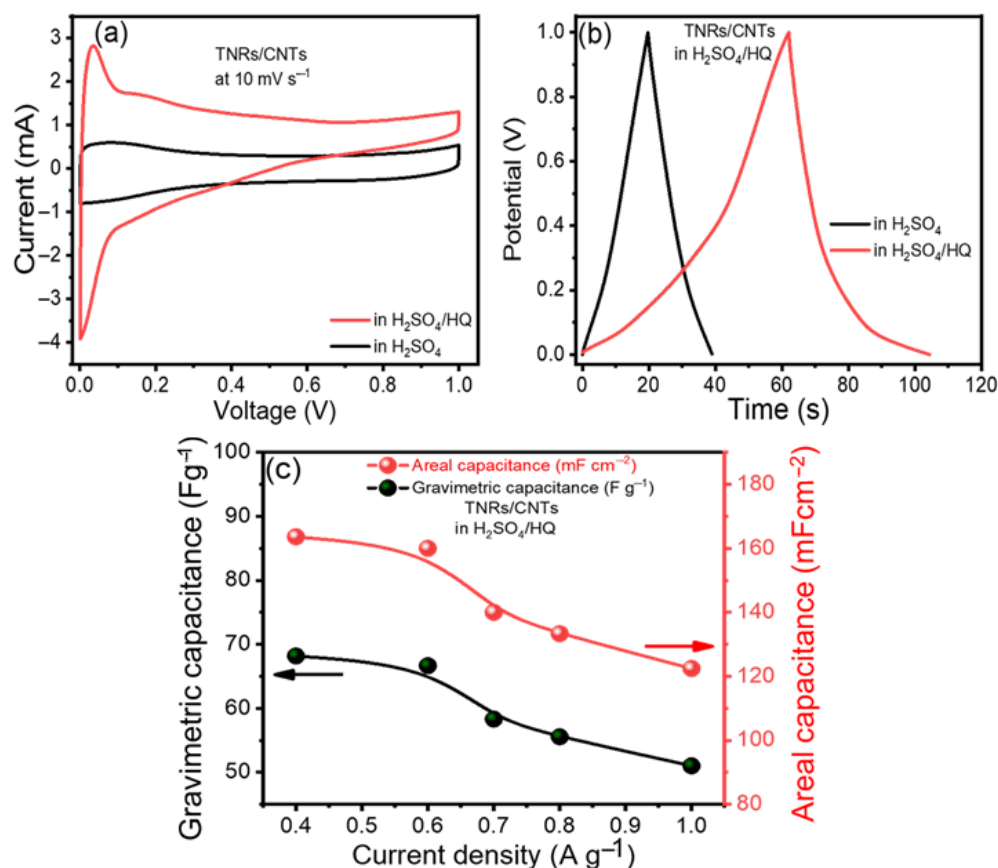


Figure 4. Electrochemical performance improvement: (a) cyclic voltammograms (CVs) and (b) charge/discharge curves (CDs) of TNR/CNTs in H_2SO_4 and a mixed electrolyte, respectively, and (c) gravimetric and areal capacitances of the TNR/CNTs in the mixed electrolyte at different current densities.

In Figure 4c, the gravimetric and areal capacitances (C_{wt} and C_{vol}) of the TNR/CNT electrodes in the mixed electrolyte ($\text{H}_2\text{SO}_4/\text{HQ}$) at various current densities are displayed, with $C_{\text{wt}} = 68.18 \text{ A g}^{-1}$ demonstrating significantly superior performance than H_2SO_4 , which was equal to 33.33 A g^{-1} . Similarly, the areal capacitance per footprint of the device

increased from 80 mF cm^{-2} in H_2SO_4 to $163.63 \text{ mF cm}^{-2}$ in $\text{H}_2\text{SO}_4/\text{HQ}$. As a result, the development of supercapacitors with our composite TNR/CNT appears promising.

EIS measurements were taken at 100 kHz to 10 mHz, which is the frequency range. These EIS measurements aided in understanding the resistive components of the supercapacitors. In EIS, Nyquist plots are useful for determining the resistivity of the electrodes. In theory, Figure 5a is divided into two regions: a high-frequency 45-degree semicircular arc and a low-frequency straight line. The charge-transfer limiting process is represented by the high-frequency arc, in which the solution resistance (R_s) is connected in series with the double-layer capacitance (C_{dl}), which is connected in parallel with the charge-transfer resistance (R_{ct}) and pseudocapacitance (C_p). The inset of Figure 5a shows the equivalent circuit provided with the values of their elements for TNR/CNTs in $\text{H}_2\text{SO}_4/\text{HQ}$. The resistance faced by the ions as they go through the separator toward the electrode surface is known as equivalent series resistance (ESR), and it may be measured at high frequency by the first intersection point on the x-axis [36]. Based on the experimental observations, as shown in the inset of Figure 5a, the ESR values for the material in H_2SO_4 and ($\text{HQ} + \text{H}_2\text{SO}_4$) were 0.54Ω and 0.51Ω , respectively. The second intersection point on the x-axis shows the charge-transfer resistance (R_{ct}), which is based on the length of the semicircular arc and is equal to the overall resistance given by the electrode/electrolyte interfaces [37]. Furthermore, R_{ct} is solely determined by the amount of active surface area on the electrode that the electrolyte can access. The length of the semicircle shown on the real axis can be used to determine R_{ct} . R_{ct} values for MWCNTs and TNR/CNTs were found to be 0.1Ω and 0.06Ω , respectively. Due to the redox behavior of the HQ, the TNRs/CNTs had a lower charge-transfer resistance, which was the same as a lower ion diffusion resistance and a higher capacitance.

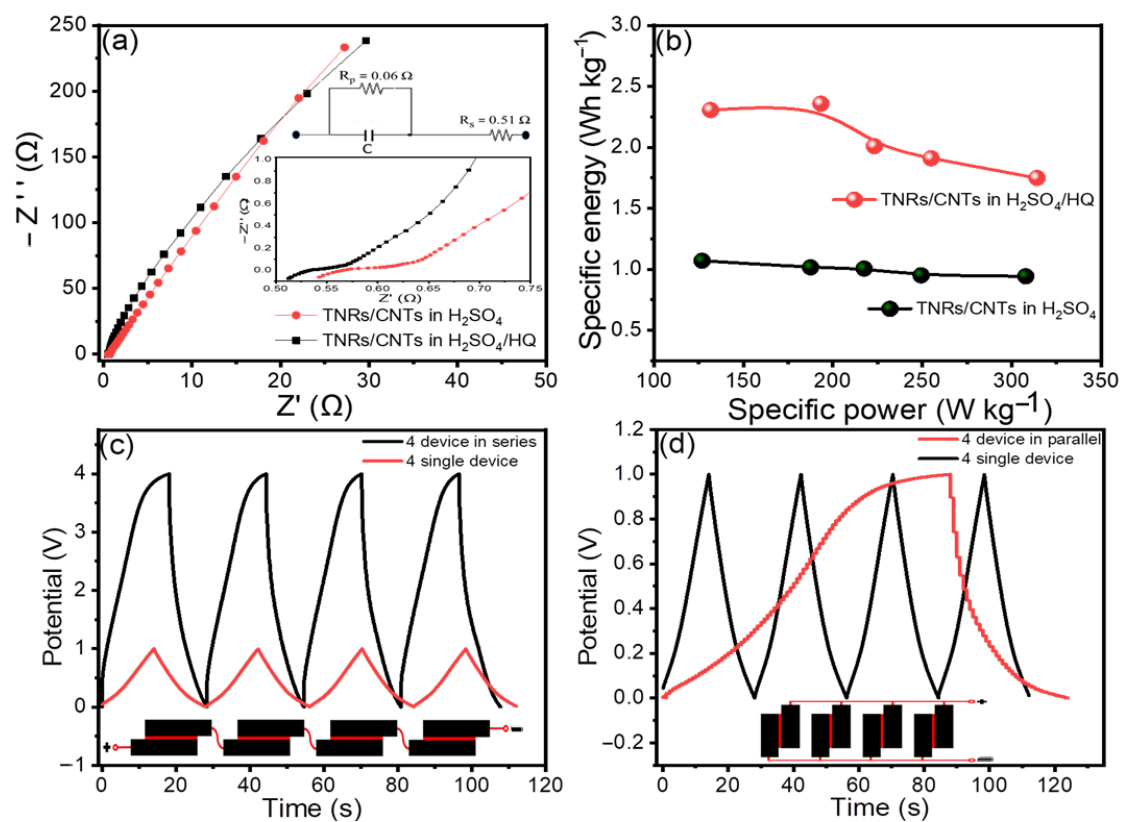


Figure 5. (a) TNR/CNT Nyquist plots in H_2SO_4 and $\text{H}_2\text{SO}_4/\text{HQ}$, respectively. The inset shows enhanced Nyquist plots in the high-frequency area; (b) a Ragone plot of specific power vs. specific energy for TNR/CNTs in H_2SO_4 and $\text{H}_2\text{SO}_4/\text{HQ}$, respectively; and CD curves of TNR/CNTs in $\text{H}_2\text{SO}_4/\text{HQ}$ for a single cell and tandem cells at 1.9 A g^{-1} (c) in series, and (d) in parallel.

Based on the total mass of electroactive materials in the two electrodes, we constructed the Ragone plot in Figure 5b with the specific energy (E_{wt}) and specific power (P_{wt}) [38].

$$E_{wt} \left(\text{Wh Kg}^{-1} \right) = \frac{0.125 C_{wt} (\Delta E)^2}{3.6} \quad (5)$$

$$P_{wt} \left(\text{W Kg}^{-1} \right) = \frac{3600 E_{wt}}{\Delta t} \quad (6)$$

The average specific energy and specific power values for the electrodes in H_2SO_4 were 1.14 Wh Kg^{-1} and 307.82 W Kg^{-1} , respectively. When $\text{H}_2\text{SO}_4/\text{HQ}$ was used as an electrolyte, much higher values of 2.35 Wh Kg^{-1} and 314.17 W Kg^{-1} were produced.

In general, a single supercapacitor's overall energy storage capacity is insufficient for most practical applications. For a specific application, a 'bank' of supercapacitors with a specific voltage and capacitance rating must be linked in series or parallel. Figure 5c,d shows the adaptability of the TNR/CNT electrodes for serial and parallel combinations by linking four devices in series and parallel configurations. This is conceivable due to the tandem TNR/CNT electrode's excellent capacity and operational voltage window being able to be controlled. Like individual supercapacitors, the tandem devices featured nearly perfect triangular charge and discharge curves, indicating good capacitive properties. This great performance was made possible without voltage balancing, which is often used with series connections to keep any cell from going into overvoltage.

The cycling performance of the cell was evaluated over 5000 cycles. The dependence of the obtained specific capacitance on the cycle number is plotted in Figure 6. Therefore, if the capacitor starts with a value of 51.02 F g^{-1} at 1 A g^{-1} , only a 2.5% loss in the capacitance is observed after about 5000 cycles. This study's cycle stability was higher than that of the other TiO_2 -based materials [7–15,39,40]. For example, after 3000 cycles, the capacitance of the TiO_2 nanocrystal in 1 M KOH electrolyte was reduced by approximately 19.4% and that of the ID TiO_2 nanotube in 1 M KOH electrolyte was reduced by approximately 33% [39,40]. The reason for this is that adding CNTs to pure TiO_2 in our electrode substantially improved the loss in capacity.

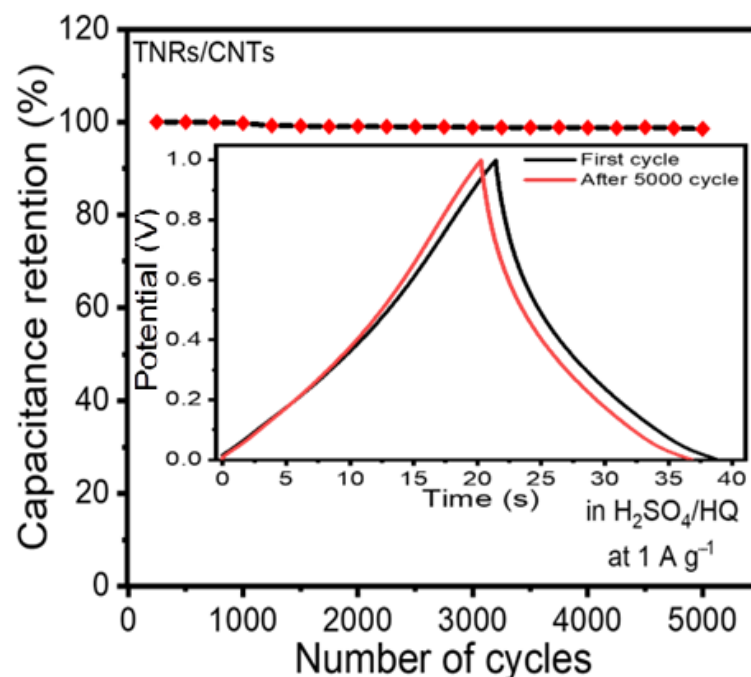


Figure 6. Stability of the electrode's performance. The electrode retained 95.5 percent of its initial capacitance after 5000 cycles. The inset shows the first and last cycle for the charge/discharge curves.

4. Conclusions

Chemical vapor deposition was used after the hydrothermal method to create titanium dioxide nanoribbons (TNRs) and multi-walled carbon nanotubes (MWCNTs). The morphological characterization proved that the MWCNTs were grown in the porous pits on the surface of one phase of the TiO₂-B nanoribbons to create a network-like structure in the nanocomposite. TNR/CNTs were used as the electrode, and H₂SO₄ or (H₂SO₄/HQ) as the electrolyte, resulting in a supercapacitor with high specific capacitance, a long cycle life, a small self-discharge process, and a high energy and power density. The TNR/CNT produced a gravimetric capacitance of 33.33 F g⁻¹ in a two-electrode supercapacitor arrangement, which was increased to 68.18 F g⁻¹ in a redox-active electrolyte of H₂SO₄/HQ. With 97.5% capacitor retention after 5000 cycles, the TNR/CNT supercapacitor also exhibited excellent cyclic stability. These findings suggest that the TNR/CNT supercapacitor may have an impact on the functionality of upcoming portable energy storage technologies.

Author Contributions: Conceptualization, M.B., M.S. and A.G.; Methodology, M.S. and A.G.; Validation, M.S. and A.G.; Formal analysis, M.S. and A.G.; Investigation, M.B., M.S. and A.G.; Resources, M.B., M.S. and A.G.; Data curation, M.B., M.S. and A.G.; Writing—original draft preparation, M.S. and A.G.; Writing—review and editing, M.B., M.S. and A.G.; Visualization, M.B., M.S. and A.G.; Project administration, M.S.; Funding acquisition, M.S. All authors have read and agreed to the published version of the manuscript.

Funding: This research received no external funding.

Institutional Review Board Statement: Not applicable.

Informed Consent Statement: Not applicable.

Data Availability Statement: Not applicable.

Conflicts of Interest: The authors declare no conflict of interest.

References

1. Kim, B.C.; Hong, J.; Wallace, G.G.; Park, H.S. Recent progress in flexible electrochemical capacitors: Electrode materials, device configuration and functions. *Adv. Energy Mater.* **2015**, *5*, 1500959. [[CrossRef](#)]
2. Béguin, F.; Presser, V.; Balducci, A.; Frackowiak, E. Supercapacitors: Carbons and electrolytes for advanced supercapacitors. *Adv. Mater.* **2014**, *26*, 2283. [[CrossRef](#)] [[PubMed](#)]
3. Wang, F.; Wu, X.; Yuan, X.; Liu, Z.; Zhang, Y.; Fu, L.; Zhu, Y.; Zhou, Q.; Wu, Y.; Huang, W. Latest advances in supercapacitors: From new electrode materials to novel device designs. *Chem. Soc. Rev.* **2017**, *46*, 6816–6854. [[CrossRef](#)] [[PubMed](#)]
4. Zeyuan, C.; Wei, B. A perspective: Carbon nanotube macro-films for energy storage. *Energy Environ. Sci.* **2013**, *6*, 3183–3201.
5. Chen, H.; Zeng, S.; Chen, M.; Zhang, Y.; Li, Q. Fabrication and functionalization of carbon nanotube films for high-performance flexible supercapacitors. *Carbon* **2015**, *92*, 271–296. [[CrossRef](#)]
6. Clement, R.C.; Prasanth, R. Advent of TiO₂ nanotubes as supercapacitor electrode. *J. Electrochem. Soc.* **2018**, *165*, E345.
7. Selvakumar, M.; Bhat, D.K. Microwave synthesized nanostructured TiO₂-activated carbon composite electrodes for supercapacitor. *Appl. Surf. Sci.* **2012**, *263*, 236–241. [[CrossRef](#)]
8. Su, H.; Wang, T.; Zhang, S.; Song, J.; Mao, C.; Niu, H.; Jin, B.; Wu, J.; Tian, Y. Facile synthesis of polyaniline/TiO₂/graphene oxide composite for high performance supercapacitors. *Solid State Sci.* **2012**, *14*, 677–681. [[CrossRef](#)]
9. Xiang, C.; Li, M.; Zhi, M.; Manivannan, A.; Wu, N. Reduced graphene oxide/titanium dioxide composites for supercapacitor electrodes: Shape and coupling effects. *J. Mater. Chem.* **2012**, *22*, 19161–19167. [[CrossRef](#)]
10. Ramadoss, A.; Kim, G.-S.; Kim, S.J. Fabrication of reduced graphene oxide/TiO₂ nanorod/reduced graphene oxide hybrid nanostructures as electrode materials for supercapacitor applications. *CrystEngComm* **2013**, *15*, 10222–10229. [[CrossRef](#)]
11. Ramadoss, A.; Kim, S.J. Improved activity of a graphene—TiO₂ hybrid electrode in an electrochemical supercapacitor. *Carbon* **2013**, *63*, 434–445. [[CrossRef](#)]
12. Sankapal, B.R.; Gajare, H.B.; Dubal, D.P.; Gore, R.B.; Salunkhe, R.R.; Ahn, H. Presenting highest supercapitance for TiO₂/MWNTs nanocomposites: Novel method. *Chem. Eng. J.* **2014**, *247*, 103–110. [[CrossRef](#)]
13. Ke, Q.; Liao, Y.; Yao, S.; Song, L.; Xiong, X. A three-dimensional TiO₂/graphene porous composite with nano-carbon deposition for supercapacitor. *J. Mater. Sci.* **2016**, *51*, 2008–2016. [[CrossRef](#)]
14. Yan, L.; Xu, Y.; Zhou, M.; Chen, G.; Deng, S.; Smirnov, S.; Luo, H.; Zou, G. Porous TiO₂ conformal coating on carbon nanotubes as energy storage materials. *Electrochim. Acta* **2015**, *169*, 73–81. [[CrossRef](#)]
15. Faraji, M. Three-dimensional nanostructures of multiwalled carbon nanotubes/graphene oxide/TiO₂ nanotubes for supercapacitor applications. *Appl. Phys. A* **2016**, *122*, 697. [[CrossRef](#)]

16. Li, Q.; Zhang, J.; Liu, B.; Li, M.; Liu, R.; Li, X.; Ma, H.; Yu, S.; Wang, L.; Zou, Y.; et al. Synthesis of High-Density Nanocavities inside TiO₂-B Nanoribbons and Their Enhanced Electrochemical Lithium Storage Properties. *Inorg. Chem.* **2008**, *47*, 9870–9873. [[CrossRef](#)] [[PubMed](#)]
17. Wen, J.; Chu, W.; Jiang, C.; Tong, D. Growth of carbon nanotubes on the novel FeCo-Al₂O₃ catalyst prepared by ultrasonic coprecipitation. *J. Nat. Gas Chem.* **2010**, *19*, 156–160. [[CrossRef](#)]
18. Vilaça, P.; Wayne, T. Friction stir welding technology. In *Structural Connections for Lightweight Metallic Structures*; Springer: Berlin/Heidelberg, German, 2011; pp. 85–124.
19. Li, Y.; Zhang, X.; Luo, J.; Huang, W.; Cheng, J.; Luo, Z.; Li, T.; Liu, F.; Xu, G.; Ke, X.; et al. Purification of CVD synthesized single-wall carbon nanotubes by different acid oxidation treatments. *Nanotechnology* **2004**, *15*, 1645. [[CrossRef](#)]
20. Mohamed, S.; Ashraf, A.M.; Abukhadra, M.R. TiO₂ nanoribbons/carbon nanotubes composite with enhanced photocatalytic activity: Fabrication, characterization and application. *Sci. Rep.* **2018**, *8*, 781.
21. Wang, Y.; Panzik, J.E.; Kiefer, B.; Lee, K.K.M. Crystal structure of graphite under room-temperature compression and decompression. *Sci. Rep.* **2012**, *2*, 520. [[CrossRef](#)]
22. Armstrong, G.; Armstrong, A.R.; Canales, J.; Bruce, P.G. Nanotubes with the TiO₂-B structure. *Chem. Commun.* **2005**, *19*, 2454–2456. [[CrossRef](#)] [[PubMed](#)]
23. Akimoto, J.; Chiba, K.; Kijima, N.; Hayakawa, H.; Hayashi, S.; Gotoh, Y.; Idemoto, Y. Soft-chemical synthesis and electrochemical property of H₂Ti₁₂O₂₅ as a negative electrode material for rechargeable lithium-ion batteries. *J. Electrochem. Soc.* **2011**, *158*, A546. [[CrossRef](#)]
24. Zhou, W.; Gai, L.; Hu, P.; Cui, J.; Liu, X.; Wang, D.; Li, G.; Jiang, H.; Liu, D.; Liu, H.; et al. Phase transformation of TiO₂ nanobelts and TiO₂ (B)/anatase interface heterostructure nanobelts with enhanced photocatalytic activity. *CrystEngComm* **2011**, *13*, 6643–6649. [[CrossRef](#)]
25. Altowyan, A.S.; Shaban, M.; Abdelkarem, K.; El Sayed, A.M. The Impact of Co Doping and Annealing Temperature on the Electrochemical Performance and Structural Characteristics of SnO₂ Nanoparticulate Photoanodes. *Materials* **2022**, *15*, 6534. [[CrossRef](#)]
26. Altowyan, A.S.; Shaban, M.; Abdelkarem, K.; El Sayed, A.M. The Influence of Electrode Thickness on the Structure and Water Splitting Performance of Iridium Oxide Nanostructured Films. *Nanomaterials* **2022**, *12*, 3272. [[CrossRef](#)] [[PubMed](#)]
27. Shaban, M.; Mona, M.; El Sayed, A.M. Structural, optical, and photocatalytic properties of the spray deposited nanoporous CdS thin films; influence of copper doping, annealing and deposition parameters. *Mater. Sci. Semicond. Process.* **2016**, *56*, 329–343. [[CrossRef](#)]
28. Gonçalves, N.; Carvalho, J.; Lima, Z.; Sasaki, J. Size-strain study of NiO nanoparticles by X-ray powder diffraction line broadening. *Mater. Lett.* **2012**, *72*, 36–38. [[CrossRef](#)]
29. Santara, B.; Giri, P.K.; Imakita, K.; Fujii, M. Evidence of oxygen vacancy induced room temperature ferromagnetism in solvothermally synthesized undoped TiO₂ nanoribbons. *Nanoscale* **2013**, *5*, 5476–5488. [[CrossRef](#)] [[PubMed](#)]
30. Pan, H.; Poh, C.K.; Feng, Y.P.; Lin, J. Supercapacitor electrodes from tubes-in-tube carbon nanostructures. *Chem. Mater.* **2007**, *19*, 6120–6125. [[CrossRef](#)]
31. Kim, K.-S.; Park, S.-J. Synthesis and high electrochemical performance of polyaniline/MnO₂-coated multi-walled carbon nanotube-based hybrid electrodes. *J. Solid State Electrochem.* **2012**, *16*, 2751–2758. [[CrossRef](#)]
32. Ko, J.M.; Kwang, S.R.; Kim, S.; Kwang, M.K. Supercapacitive properties of composite electrodes consisting of polyaniline, carbon nanotube and RuO₂. *J. Appl. Electrochem.* **2009**, *39*, 1331–1337. [[CrossRef](#)]
33. Shao, Y.; El-Kady, M.F.; Lin, C.-W.; Zhu, G.; Marsh, K.L.; Hwang, J.Y.; Zhang, Q.; Li, Y.; Kaner, R.B. 3D freeze-casting of cellular graphene films for ultrahigh-power-density supercapacitors. *Adv. Mater.* **2016**, *28*, 6719–6726. [[CrossRef](#)]
34. Tao, Y.; Xie, X.; Lv, W.; Tang, D.; Kong, D.; Huang, Z.; Nishihara, H.; Ishii, T.; Li, B.; Golberg, D.; et al. Towards ultrahigh volumetric capacitance: Graphene derived highly dense but porous carbons for supercapacitors. *Sci. Rep.* **2013**, *3*, 2975. [[CrossRef](#)] [[PubMed](#)]
35. Roldán, S.; Blanco, C.; Granda, M.; Menéndez, R.; Santamaria, R. Towards a further generation of high-energy carbon-based capacitors by using redox-active electrolytes. *Angew. Chem. Int. Ed.* **2011**, *50*, 1699–1701. [[CrossRef](#)] [[PubMed](#)]
36. Kötz, R.; Carlen, M. Principles and applications of electrochemical capacitors. *Electrochim. Acta* **2000**, *45*, 2483–2498. [[CrossRef](#)]
37. Rakhi, R.B.; Chen, W.; Hedhili, M.N.; Cha, D.; Alshareef, H.N. Enhanced rate performance of mesoporous Co₃O₄ nanosheet supercapacitor electrodes by hydrous RuO₂ nanoparticle decoration. *ACS Appl. Mater. Interfaces* **2014**, *6*, 4196–4206. [[CrossRef](#)]
38. Wang, K.; Wu, H.; Meng, Y.; Zhang, Y.; Wei, Z. Integrated energy storage and electrochromic function in one flexible device: An energy storage smart window. *Energy Environ. Sci.* **2012**, *5*, 8384–8389. [[CrossRef](#)]
39. Patil, J.V.; Mali, S.S.; Shaikh, J.S.; Bhat, T.S.; Hong, C.K.; Kim, J.H.; Patil, P.S. Hydrothermally grown 3D hierarchical TiO₂ based on electrochemically anodized 1D TiO₂ nanostructure for supercapacitor. *Appl. Phys. A* **2018**, *124*, 592. [[CrossRef](#)]
40. Heng, I.; Lai, C.W.; Juan, J.C.; Numan, A.; Iqbal, J.; Teo, E.Y.L. Low-temperature synthesis of TiO₂ nanocrystals for high performance electrochemical supercapacitors. *Ceram. Int.* **2019**, *45*, 4990–5000. [[CrossRef](#)]

Disclaimer/Publisher’s Note: The statements, opinions and data contained in all publications are solely those of the individual author(s) and contributor(s) and not of MDPI and/or the editor(s). MDPI and/or the editor(s) disclaim responsibility for any injury to people or property resulting from any ideas, methods, instructions or products referred to in the content.